

Surface brightness profiles of blue compact dwarf galaxies in the GOODS-N and GOODS-S field

J. H. Lian^{*}, X.Kong, N.Jiang, W. Yan and Y. L. Gao

Department of Astronomy, University of Science and Technology of China, Hefei 230026, China

Key Laboratory for Research in Galaxies and Cosmology, Chinese Academy of Sciences, Hefei 230026, China

6 January 2016

ABSTRACT

We investigate the structural properties of the underlying hosts of 34 blue compact dwarf (BCD) galaxies with deep near-infrared (NIR) photometry. The BCD sample is selected from the Cosmic Assembly Near-IR Deep Extragalactic Legacy Survey in the Great observatories origins Deep Survey North and South fields. We extract the surface brightness profile (SBP) in the optical $F435W$ and NIR $F160W$ bands. The SBPs of BCDs in the H band reach ~ 26 mag arcsec⁻² at the 3σ level, which is so far the deepest NIR imaging of BCDs. Then we fit the SBPs with one- and two-component Sérsic models. About half of the BCDs favour the two-component model which significantly improves the fit quality. The effective radii of the underlying hosts of BCDs in the B band are smaller than those of early-type dwarfs (dEs) and dwarf irregulars at a fixed luminosity. This discrepancy is similar to findings in many previous works. However, the difference in structural parameters between BCDs and other dwarf galaxies seems to be less significant in the H band. Furthermore, we find a remarkable agreement between the underlying hosts of BCDs and dEs. All dwarf galaxies seem to follow a similar luminosity-radius relationship which suggests a unified structural evolution for dwarf galaxies. We conclude that a possible evolution track from BCDs to dEs cannot be ruled out, with no significant change of structure needed in the evolutionary scenario.

Key words: galaxies: dwarf – galaxies: evolution – galaxies: photometry – galaxies: structure

1 INTRODUCTION

Blue compact dwarf (BCD) galaxies are compact and low-luminosity ($M_B \geq -17$ mag) objects, which are undergoing active star formation at the present time (Sargent & Searle 1970; Kunth & Östlin 2000). They are believed to be part of the building blocks of massive galaxies in the early Universe. The gas consumption time-scale of BCDs, given the current star formation rate, is much shorter than the age of the Universe (Kong 2004). BCDs and dwarf irregulars (dIrrs) are chemically unevolved and metal-poor ($Z_{\odot}/50 \leq Z \leq Z_{\odot}/3$) galaxies, early-type dwarfs (dEs) have a considerable spread in metallicity (Kunth & Östlin 2000). Some extremely metal-poor BCDs were initially considered to be young galaxies with their first generation of stars forming. However, subsequent detection of the underlying extended old stellar population in most BCDs indicates that they are actually old systems (Papaderos et al. 1996; Cairós et al. 2003; Kong et

al. 2003). The underlying old populations of BCDs are often regarded as the ‘underlying host’ of the central star-forming region.

The evolutionary relationship between BCDs and other dwarf galaxies is not clear and still under debate. A possible evolution scenario, proposed by Thuan (1985) and Davies & Phillipps (1988), is that dIrrs evolve into BCDs in several starbursts, enrich the interstellar, exhaust their gas and then fade to gas-free dEs. Later on, Papaderos et al. (1996) discussed the possible evolutionary connections between BCDs and other dwarf galaxies and suggested that the stellar wind from the central starburst is necessary to explain the compactness and central brightness of BCDs. Recently, Janowiecki & Salzer (2014) compared the structural properties of the underlying hosts of BCDs in the optical and near-infrared (NIR) bands with those of dIrrs. They fit the outer regions of BCDs exponentially and found that the underlying hosts of BCDs are brighter in the centre and have smaller radii than dIrrs. They concluded that, if BCDs can evolve into dIrrs, some physical mechanism should be responsible for the significant change of structural

^{*} E-mail:ljhhw@mail.ustc.edu.cn (JHL); xkong@ustc.edu.cn (XK)

properties from BCDs to dIrrs. A different result was found by Micheva et al. (2013) with deep imaging of luminous dwarf galaxies and intermediate-mass BCGs. They measured the structural parameters of the underlying hosts of BCGs with surface brightness in the B band μ_B in the range 26–28 mag arcsec⁻² and found that the hosts of BCGs have similar structural parameters with other dwarf galaxies like dEs and dIrrs. They suggested that the obtained structural properties for surface brightness μ_B in 24–26 mag arcsec⁻² range are possibly affected by nebular emission from central star-forming regions. It should be noted that the depth of the B band image in Janowiecki & Salzer (2014) only reaches ~ 26 mag arcsec⁻². Meanwhile, a fit only to the outer region of a galaxy may be sensitive to the selection of the inner boundary of the fit.

Meyer et al. (2014) determined the structural properties of the underlying host of BCDs and dEs in the Virgo Cluster and also found the BCD hosts to be smaller than the dIrrs. However, they argued in addition that the BCD hosts and dIrrs together are largely overlapping with the structural parameters of dEs. Moreover, the overlapping will be more significant if the different distance of each BCD from the Virgo Cluster centre are taken into consideration.

Since NIR light traces the old stellar population, many authors have used deep NIR imaging to study the structural properties of the underlying hosts of dwarf galaxies (Cairós et al. 2003; Micheva et al. 2013; Janowiecki & Salzer 2014; Janz et al. 2014; Young et al. 2014). However, the deepest NIR images (usually H band) only reach ~ 23 mag arcsec⁻² for BCDs (Micheva et al. 2013) and ~ 24 mag arcsec⁻² for other dwarf galaxies (Janz et al. 2014; Young et al. 2014). To probe the underlying host of BCDs at larger radii and better constrain their structural properties, deeper NIR images are needed. The Cosmic Assembly Near-IR Deep Extragalactic Legacy Survey (CANDELS, Grogin et al. 2011; Koekemoer et al. 2011) obtained extremely deep images of galaxies with the Wide Field Camera 3 (WFC3/IR) and the Advanced Camera for Surveys on the *Hubble Space Telescope* (*HST*), which have a full width at half-maximum (FWHM) of ~ 0.13 arcsec at NIR. The survey targets five sky regions. Among them, the Great Observatories Origins Deep Survey North and South fields (GOODS-N and GOODS-S) are two sky regions with deeper NIR imaging than the other three. This deep NIR photometry survey allows detailed analysis of the structural properties of dwarf galaxies outside our nearby Universe. In this work, we select a BCD sample from the CANDELS GOODS-N and GOODS-S fields and study the structural properties of the underlying hosts of these BCDs.

Throughout this paper, we adopt the cosmological parameters $H_0 = 70$ km s⁻¹ Mpc⁻¹, $\Omega_\Lambda = 0.73$ and $\Omega_m = 0.27$. All magnitudes in this paper are given in the AB photometric system unless otherwise stated.

2 SAMPLE SELECTION

There are many definitions of BCDs according to their distinctive spectral features or morphological properties. The widely used definition in Gil de Paz et al. (2003) defines galaxies with the following properties as BCDs: the galaxy is 1) blue with $B - R < 1$; 2) compact with peak surface brightness in the B band $\mu_{\text{peak}} < 22$ mag arcsec⁻²; 3) a dwarf

with $M_K > -21$ mag. In this work, we select BCDs in the GOODS-N and GOODS-S fields from the WFC3-selected photometry catalogue of Skelton et al. (2014) and Brammer et al. (2012). We use the definition in Gil de Paz et al. (2003) but parametrize ‘dwarf’ via the stellar mass determined by fitting the spectral energy distributions from optical to NIR (Skelton et al. 2014). To obtain a BCD sample with robust stellar mass and physical size estimation, spectroscopic redshift is needed. Considering the redshift dimming effect, the low surfaces of galaxies are not detectable at high redshift. Therefore, only galaxies with $z < 0.25$ are selected. Our final selection criteria for BCD are: 1) peak surface brightness at *HST F435W* $\mu_{\text{peak}} < 22$ mag arcsec⁻²; 2) restframe colour of $B - R < 1$; 3) stellar mass $M_* < 10^9 M_\odot$; 4) redshift $z < 0.25$. Finally, 20 galaxies in the GOODS-N field and 14 in the GOODS-S field are selected as BCD via spectroscopic redshift measurement. Stellar mass and spectroscopic redshift are taken from the catalogue of Skelton et al. (2014), who estimate stellar mass by using FAST code (Kriek et al. 2009) and compile spectroscopic redshift from literature. The *HST F160W* and *F435W* band images of these BCDs are shown in Figs. 1 and 2 with an image size of 100 arcsec \times 100 arcsec (Skelton et al. 2014)¹.

The basic properties of the BCD sample are listed in Table 1. We also calculate the rotational asymmetry of BCDs by using the publicly available code, MORPHEUS (Abraham et al. 2007). The asymmetry is measured by rotating the galaxy image by 180° and subtracting it from the original image (Conselice 2003). For simplicity, object IDs in the GOODS-N field are prefixed with ‘GN’ and in the GOODS-S field with ‘GS’.

3 SURFACE BRIGHTNESS PROFILES AND FITTING

In this paper, we focus on the structural properties of underlying hosts of BCDs at *HST F435W* and *F160W* bands. We run the Image Reduction and Analysis Facility (IRAF) Ellipse task (Jedrzejewski 1987) to fit elliptical isophotes to the images and measure the light profiles. Ellipse fit the isophotes from the centre towards the outskirts along the semimajor axes with step size of 1 pixel. We use the SEXTRACTOR program (Bertin & Arnouts 1996) to distinguish objects that do not belong to the BCD and then mask them out. The geometric parameters (centre, ellipticity and position angle) are obtained by following the procedure in Li et al. (2011). First, we run Ellipse and set all three geometry parameters free. The centre of the BCD is the average central position of ellipses within ~ 0.3 – 0.6 arcsec. Then, we fix the centre to the value just obtained and run Ellipse again, while the ellipticity and position angle are still set free. Typically we calculate these two parameters as the average value at the outer regions of the galaxy, where the intensity is about three times above the sky. Finally, we run Ellipse to obtain the surface brightness profiles (SBPs), fixing the geometric parameters to the values obtained above. We estimate the sky background noise by binning the sky

¹ We use *F160W* and *F435W* mosaics from 3D-HST website <http://3dhst.research.yale.edu/Home.html>

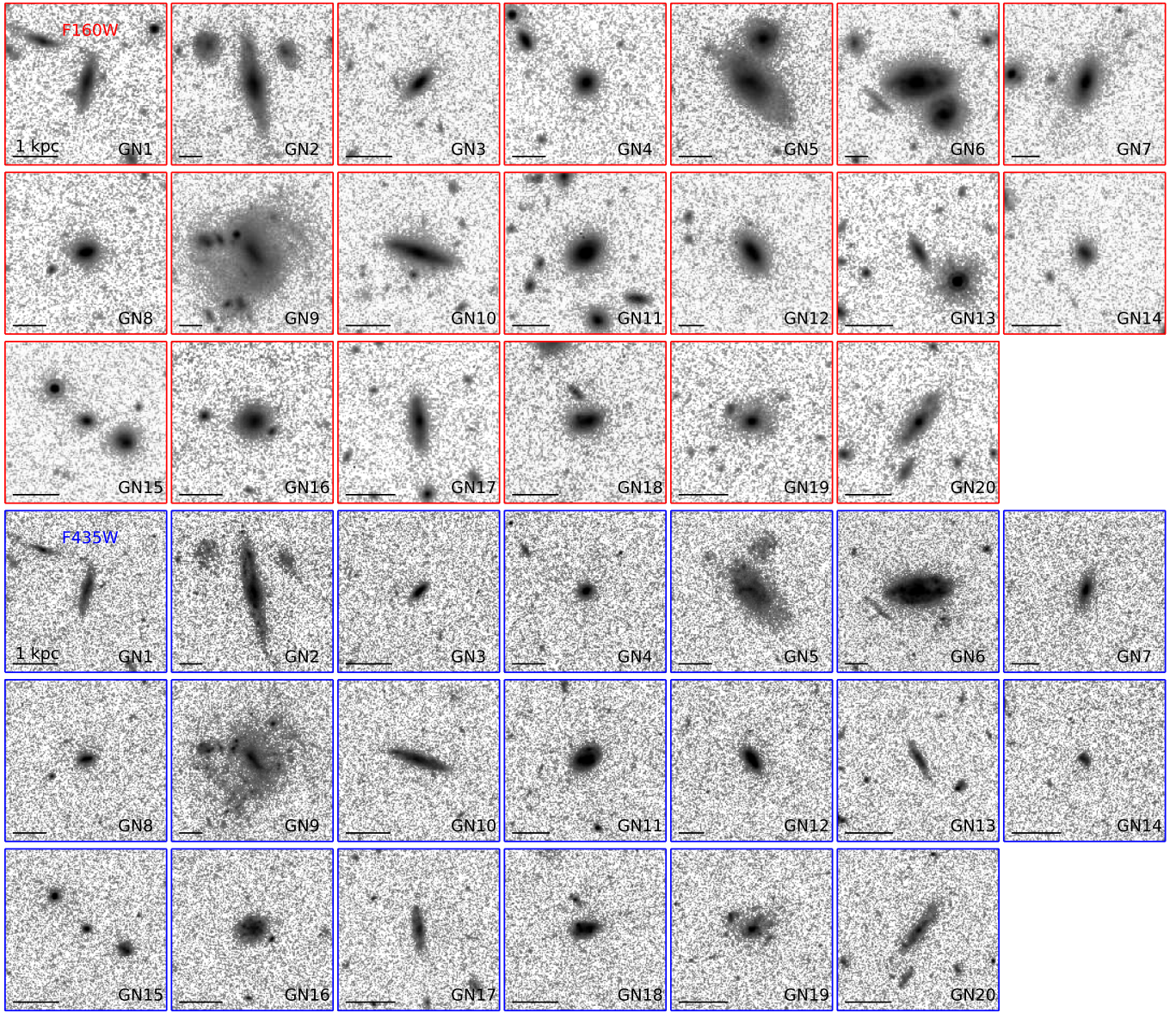


Figure 1. $F435W$ and $F160W$ images of BCDs in the GOODS-N field with logarithmic gray-scale. Upper three rows are for BCDs in the $F160W$ band and bottom three rows for the $F435W$ band.

The image size is $100 \text{ arcsec} \times 100 \text{ arcsec}$. Length of the solid line in the bottom left of each panel indicates the size of 1 kpc at the redshift of the BCD. $F160W$ images have red frames while $F435W$ image frames are blue. Each panel is marked with the object ID.

background pixel (galaxies and stars are masked out) with bin size comparable to the size of the object and calculating the variance of values in all bins. The surface brightness uncertainties are the quadratic sum of those in the Ellipse result with the sky background noise just determined. A signal-to-noise ratio criterion ($\text{SN} > 3$) for isophote is set to obtain the SBP.

The obtained SBPs are shown in Figs. 3 and 4 for BCDs in the GOODS-N and GOODS-S fields, respectively. Ellipticity and position angle values are shown in the upper right corner. The squares in each panel represent the SBPs in the $F435W$ band and the circles represent SBPs in the $F160W$ band. In the case of the BCD GS2, which has extremely irregular morphology in the $F435W$ band, no reliable SBP can

be extracted from the $F435W$ image. The surface brightness is corrected for the redshift dimming effect by a factor of $(1+z)^4$. It can be seen that the surface brightness in the $F160W$ band reaches $\sim 26 \text{ mag arcsec}^2$ which is $\sim 1.5 \text{ mag}$ deeper than the deepest NIR photometry of BCDs. The CANDELS survey is much deeper than the previous NIR photometry of dwarf galaxies and can detect the outskirts at larger radius, which may be essential to constrain the structural properties of the underlying old stellar population. We also plot $B - H$ colour versus radius in the bottom of each panel. The colour profiles are generally flat or ascending with radius.

In some cases, there are some bumps in the SBPs. It can be seen that the SBP tends to be smoother in the $F160W$

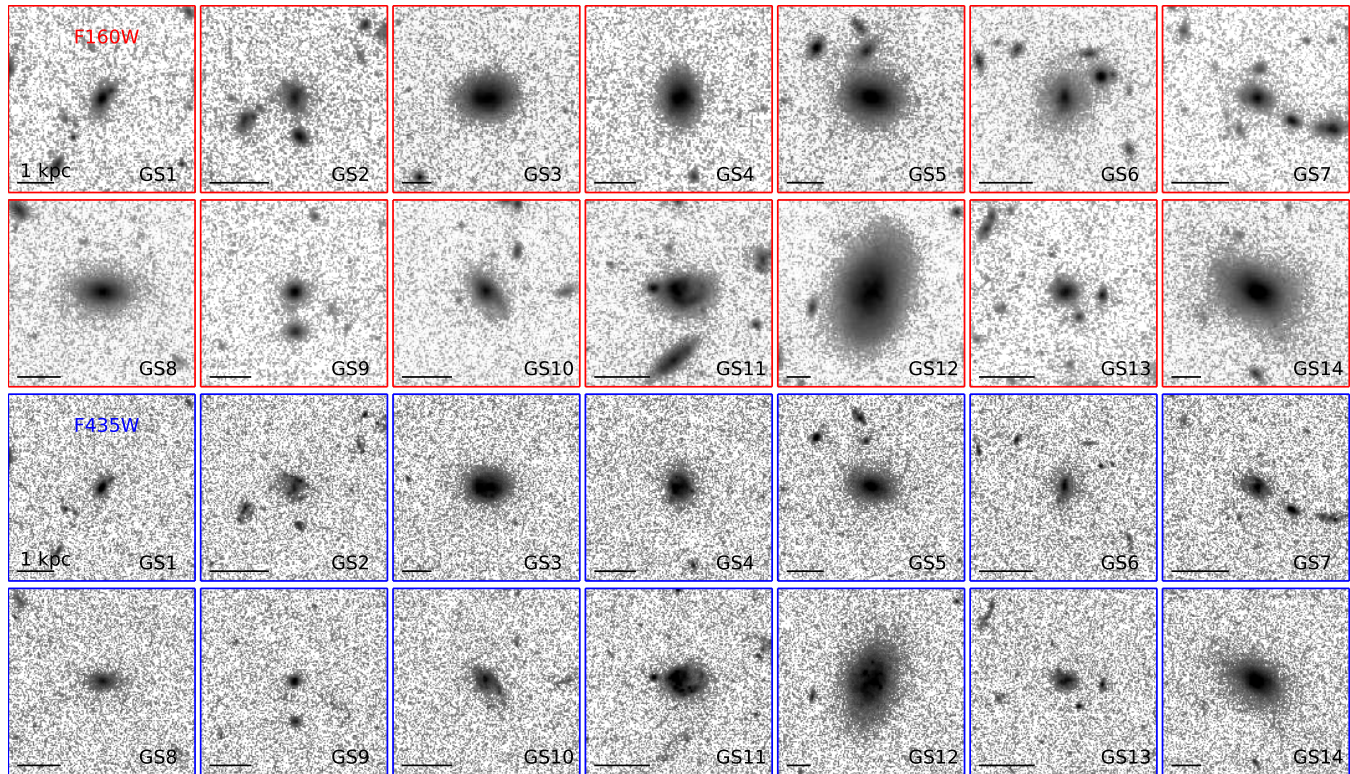


Figure 2. Same as Fig. 1 but with BCD sample in the GOODS-S field.

than in the $F435W$ band. Meanwhile, asymmetry of BCDs at $F160W$ band are generally lower than that at $F435W$ band. Therefore, these bumps in the SBPs are possibly due to distribution of star formation regions in the outskirts. The asymmetry of BCDs in the $F435W$ band seems to be much lower than the massive starburst galaxies, such as ultraluminous infrared galaxies (Conselice 2003). There are two emission lines from star forming regions that could have possibly affected the observed H -band photometry of our sample: $[\text{Fe II}]$ at $1.25 \mu\text{m}$ and $\text{Pa } \beta$ at $1.28 \mu\text{m}$. However, the equivalent widths (EWs) of these two lines are generally low. For typical NIR spectra of HII galaxies (Martins et al. 2013) and irregular galaxies (Mannucci et al. 2001), the EWs are less than 10 \AA . Besides, we might expect that the emission lines could be more weak in the outskirts of BCDs. Therefore, the SBP in the H band will not be significantly affected by star forming regions.

There are many functions that can be used to fit the SBP of a galaxy. The most widely-used is the Sérsic function:

$$I(r) = I_e \exp(-b_n [(r/r_e)^{1/n} - 1]) \quad (1)$$

with intensity I_e at r_e . The effective radius r_e is the radius that encloses half of the total luminosity of the galaxy. The Sérsic index n indicates the steepness of the profile. Approximation of the constant, b_n as $1.9992n - 0.3271$, is valid for $0.5 < n < 10$ (Prugniel & Simien 1997). The SBPs of dwarf galaxies are usually fit with an exponential function (i.e., $n = 1$ in Eq. 1):

$$I(r) = I_0 \exp(-\frac{r}{h}) \quad (2)$$

with intensity I_0 at the centre, and scalelength h (see Gra-

ham & Driver 2005 for the transformation between scalelength h and effective radius r_e).

Two models are used to fit the SBPs: a one-component Sérsic model and a two-component model combining an inner Sérsic component and an outer exponential component. Although the two-component model is more flexible and always fits the SBPs better, we need to quantify the fit quality to quantitatively justify whether the two-component decomposition is indeed needed. The fit quality Q is defined as the weighted quadratic sum of the difference between observed and best-fitting model SBP

$$Q = \sum_i \frac{1}{\sigma_i} \sum_j \frac{1}{\sigma_j} (\mu_{\text{obs},i} - \mu_{\text{fit},i})^2, \quad (3)$$

where σ are the uncertainties of observed surface brightness, μ_{obs} . The summation is carried out over the SBP. We fit the SBPs with the two models using the IDL routine MPFIT (Markwardt 2009). There are three free parameters in the Sérsic function: surface brightness at effective radius μ_e , Sérsic index n and effective radius r_e . The initial values are arbitrarily chosen to be $\mu_e = 21 \text{ mag arcsec}^{-2}$, $n = 1$ and $r_e = 10$ pixels. The surface brightness uncertainties are used for weighting with weight values of $1/\sigma^2$.

For the $F435W$ band, we fit the SBPs of BCDs with both the one- and two-component models. For the two-component model, the blue dot-dashed and dashed lines in Figs. 3 and 4 represent the Sérsic and exponential components, respectively. The blue solid lines represent their sum. The best-fitting parameters are listed in Table 2. The ‘ Q ’ column shows fit quality result, with a lower value of this quantity suggesting a better fit. It is obvious that the two-component model yields a ‘better fit quality’ in most cases.

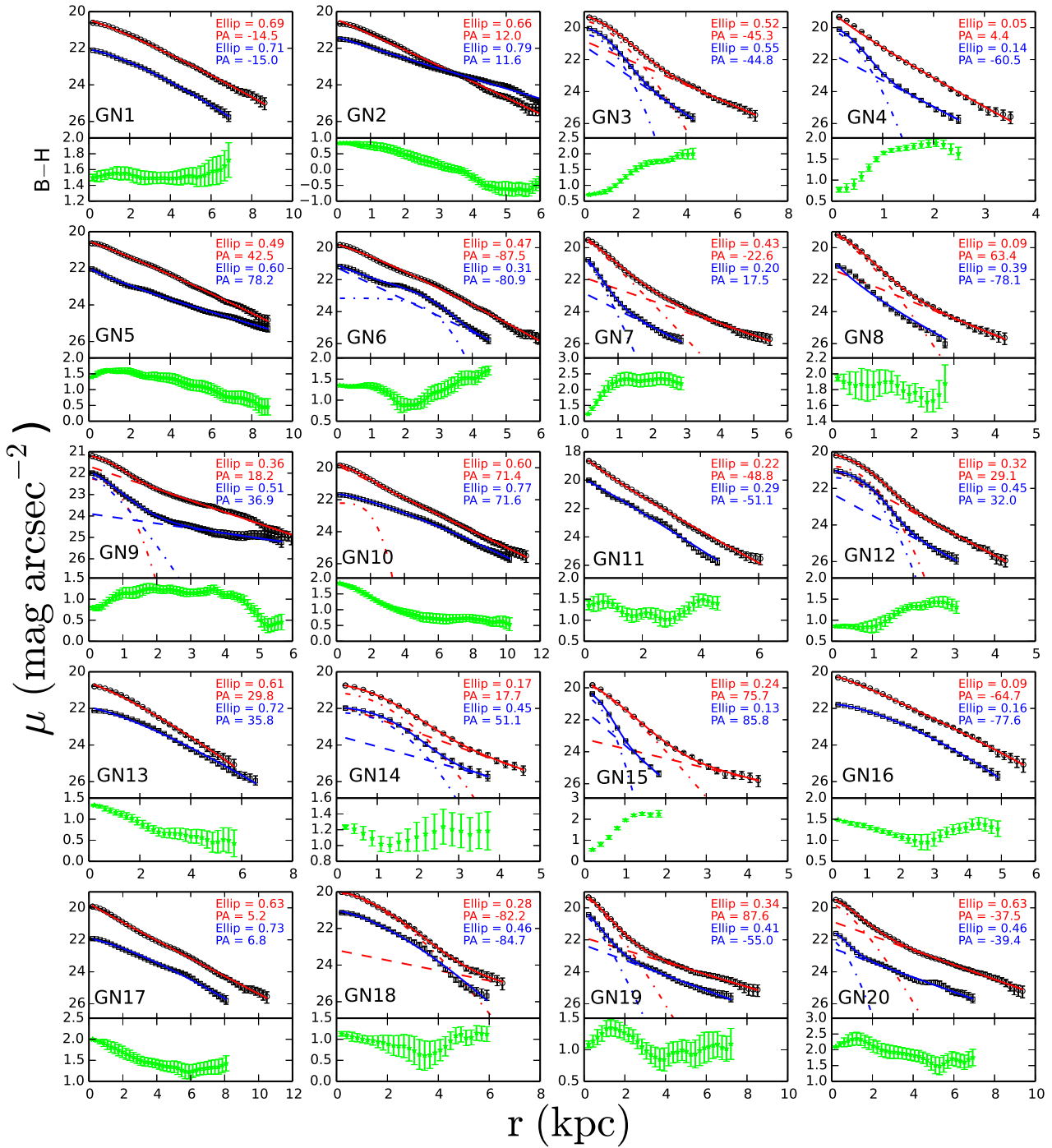


Figure 3. SBPs of BCDs in the $F160W$ (circles) and $F435W$ (squares) bands. The best-fitting model is shown as solid lines. If the two-component model are used, the two components are shown as dashed and dot-dashed lines. Some BCDs are well-fitted with one-component model and only solid lines are plotted in these panels. The bottom of each panel shows $B-H$ colour profiles. Each panel is marked with the object ID. Ellipticity and position angle values are shown in the upper right corner. The upper two quantities are obtained in the $F160W$ band and the bottom two quantities with blue colour are for $F435W$ band.

Table 1. Basic properties of BCD sample.

ID	RA (J2000) (h:m:s)	Dec. (J2000) ($^{\circ}$ ' ")	m _{F435W} (mag)	m _{F160W} (mag)	z ^a	log(M _{star}) (M _⊙)	$B - H$ ^b (mag)	Asym435 ^c	Asym160
GN1	12:36:26.03	62:07:50.9	23.00±0.01	21.36±0.01	0.20	8.66	1.15	0.07	0.05
GN2	12:36:43.35	62:08:19.3	21.52±0.01	20.53±0.01	0.09	8.21	0.85	0.11	0.04
GN3	12:36:51.12	62:09:38.6	22.27±0.00	21.27±0.01	0.21	8.41	0.74	0.14	0.09
GN4	12:36:51.65	62:09:54.6	22.14±0.01	21.01±0.00	0.14	8.41	1.06	0.13	0.10
GN5	12:36:32.46	62:10:37.4	21.60±0.01	19.95±0.01	0.14	8.90	1.24	0.11	0.07
GN6	12:36:41.63	62:11:31.8	20.79±0.00	19.56±0.00	0.09	8.70	0.97	0.35	0.12
GN7	12:37:18.29	62:11:50.7	22.25±0.00	20.69±0.00	0.11	8.40	1.45	0.07	0.03
GN8	12:36:06.38	62:12:53.1	22.95±0.01	20.77±0.00	0.14	8.75	1.82	0.06	0.04
GN9	12:36:59.39	62:14:04.8	21.01±0.01	19.94±0.01	0.09	8.46	0.99	0.14	0.10
GN10	12:36:43.75	62:13:56.8	22.32±0.01	20.48±0.00	0.20	8.96	1.25	0.07	0.06
GN11	12:36:17.42	62:14:16.4	21.46±0.00	19.97±0.00	0.16	8.98	1.22	0.17	0.05
GN12	12:36:56.50	62:14:19.9	21.66±0.00	20.69±0.00	0.10	8.21	0.99	0.13	0.05
GN13	12:37:29.99	62:15:59.6	23.63±0.01	22.30±0.01	0.22	8.35	0.89	0.10	0.04
GN14	12:36:30.39	62:15:58.7	23.63±0.01	22.26±0.01	0.23	8.12	0.97	0.12	0.05
GN15	12:36:51.47	62:17:33.2	23.47±0.01	22.36±0.01	0.21	8.27	0.91	0.22	0.05
GN16	12:37:57.07	62:18:05.0	22.26±0.01	20.87±0.01	0.19	8.80	0.98	0.17	0.07
GN17	12:37:08.82	62:18:18.0	23.14±0.01	21.16±0.01	0.23	8.84	1.42	0.11	0.08
GN18	12:37:25.44	62:19:08.0	21.97±0.00	20.83±0.01	0.21	8.59	0.70	0.32	0.09
GN19	12:37:21.25	62:19:15.5	22.61±0.01	21.24±0.01	0.23	8.47	0.84	0.15	0.08
GN20	12:37:21.71	62:20:05.3	23.31±0.01	21.22±0.01	0.21	8.80	1.29	0.11	0.07
GS1	03:32:36.98	-27:55:24.1	22.56±0.00	21.74±0.01	0.13	8.04	0.75	0.18	0.10
GS2	03:32:49.75	-27:54:03.9	23.27±0.01	21.83±0.02	0.24	8.61	0.78	0.20	0.06
GS3	03:32:42.55	-27:52:52.3	21.12±0.00	20.06±0.00	0.10	8.48	0.91	0.10	0.06
GS4	03:32:42.81	-27:52:40.6	21.82±0.00	20.30±0.01	0.15	8.99	1.22	0.25	0.05
GS5	03:32:52.12	-27:51:08.7	21.08±0.02	19.80±0.00	0.13	8.88	1.20	0.09	0.04
GS6	03:32:40.79	-27:50:35.1	22.55±0.01	21.37±0.01	0.21	8.61	0.80	0.11	0.06
GS7	03:32:11.38	-27:49:17.8	22.69±0.01	21.89±0.01	0.23	8.37	0.43	0.12	0.03
GS8	03:32:48.91	-27:49:05.2	22.93±0.01	20.91±0.01	0.16	8.73	1.50	0.06	0.05
GS9	03:32:53.75	-27:48:51.0	23.45±0.01	21.98±0.01	0.15	8.16	1.18	0.11	0.11
GS10	03:32:25.13	-27:47:24.3	22.99±0.01	21.67±0.01	0.19	8.39	0.70	0.09	0.07
GS11	03:32:19.18	-27:44:46.3	21.16±0.00	20.40±0.00	0.22	8.69	0.46	0.37	0.32
GS12	03:32:28.34	-27:44:26.2	20.37±0.00	19.27±0.00	0.08	8.62	0.99	0.28	0.04
GS13	03:32:19.25	-27:44:38.9	23.20±0.01	21.92±0.01	0.22	8.44	0.70	0.09	0.08
GS14	03:32:33.39	-27:43:49.1	20.84±0.00	19.53±0.00	0.10	8.63	1.18	0.11	0.06

Notes: ^a Redshift.^b Global $B - H$ colour using total magnitude.^c Asymmetry is given for both bands in the two last columns.

However, in some cases, where the fit quality of the one-component model is relatively high or the number of data points is limited, the two-component model will yield unphysical parameter values in either the Sérsic or the exponential component. Moreover, the improvement in fit quality using the two-component model is always limited in these cases. For 10 BCDs in GOODS-N and 7 BCDs in GOODS-S, we use the parameters of the one-component model for comparison. The preference of decomposition is listed in the last column of Table 2. The absolute magnitude is calculated by integrating the best-fitting profile from centre to infinity (Young et al. 2014). The $F435W$ and $F160W$ bands trace the young and old stellar population of galaxies, respectively, and roughly correspond to the B and H bands of the ground-based photometry system. We do k -corrections for $F435W$ and $F160W$ bands by applying a correction factor of the difference between the observed $F435W$ or $F160W$ magnitude and the restframe B or H band magnitude. These magnitudes are all taken from the catalogue of Skelton et al. (2014). It should be noted that the spatial resolution is higher in the $F435W$ band images (FWHM of ~ 0.06 arcsec)

than in the $F160W$ band images (FWHM of ~ 0.15 arcsec). To explore the resolution effect, we impose an additional Gaussian filter to the $F435W$ band images and reduce the resolution to the level of the $F160W$ band images. Then we obtain the structural parameters by the same procedure described above. The discrepancy between structural parameters of low and high resolution images is generally small.

For the $F160W$ band, both the one- and two-component models are used for fitting and comparison with other dwarf galaxies. The best-fitting parameters are listed in Table 3. The dot-dashed and dashed red lines in Figs. 3 and 4 show the Sérsic and exponential components in the two-component fitting. The red solid lines represent their sum. It can be seen that for the most part the two-component model fits the SBP of BCDs better than the one-component model. For 10 BCDs in GOODS-N and 5 in GOODS-S we use the parameters of the one-component model, which is more robust than the two-component model, for comparison at H band. Janowiecki & Salzer (2014) fit the outer region of BCDs with an exponential function. They argued that the outer regions of BCDs have colours consistent with

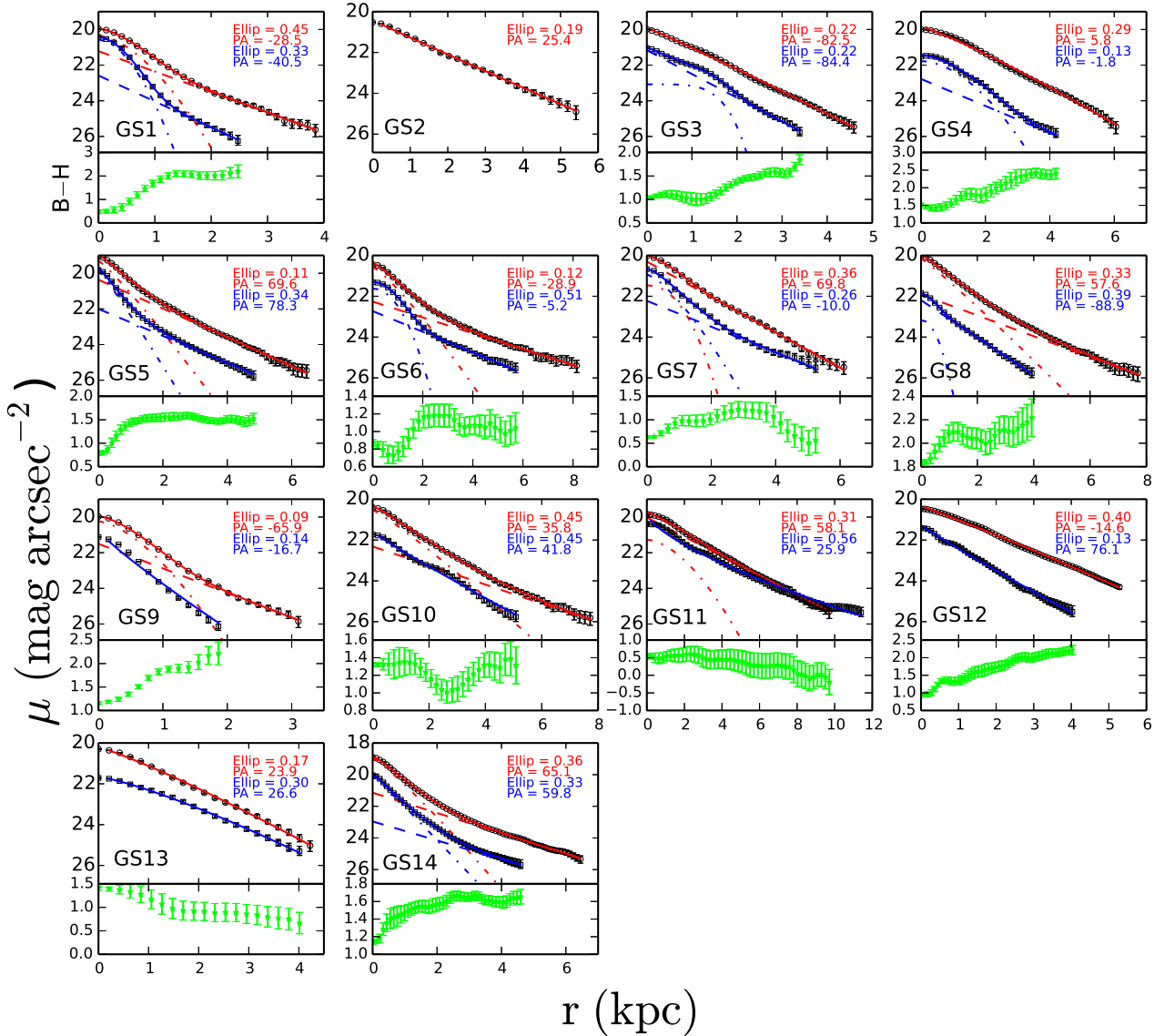


Figure 4. Same as Fig. 3 but with BCD sample in the GOODS-S field.

evolved stellar populations by comparing the $B-H$ colour of the outer region with simple stellar population models. For BCDs with moderately low metallicities, the outer regions have colours at ~ 2.5 mag in the Vega photometric system. It can be seen in the colour profiles in Figs. 3 and 4 that, for the outer regions of BCDs where the exponential component dominates the SBP, the $B-H$ colour is almost redder than 1.0 mag, which correspond to ~ 2.3 mag in the Vega photometric system. Therefore, the outer regions of BCDs are generally dominated by evolved stellar populations and the exponential component mainly reflects the SBP of the underlying host of the BCD. However, the inner Sérsic component may not correspond to the star forming region at the centre.

4 COMPARISON WITH OTHER DWARF GALAXIES

In Fig. 5, we compare the structural parameters of our BCDs to those for the dwarf galaxies in the literature in the B band. To be consistent with previous works where only the parameters for the outer regions of galaxies are measured, we use the exponential components of our BCDs for comparison. As discussed in Section 3, the parameters of the one-component model are used instead for 17 BCDs where that model is sufficient. Blue circles represent BCDs at a redshift of 0.09–0.15 and are marked as ‘BCDz1’. Red circles show BCDs at redshift of 0.15–0.25 and are marked as ‘BCDz2’. Although BCDs at the higher redshift range tend to be brighter which could possibly be due to a selection effect, all BCDs at the two redshift ranges are on the same sequence of luminosity-radius relationship. We include the

structural parameters of dwarf galaxies in the B band compiled from the literature in the comparison. Black crosses in Fig. 5 are BCDs from Marlowe et al. (1997) and Cairós et al. (2001). Purple triangles are dIrrs from Patterson & Thuan (1996) and van Zee (2000) and green squares are dEs from Binggeli & Cameron (1993). The magnitudes in the literature are converted from the Vega to the AB photometric system with a conversion factor of -0.163 mag in the B band. The absolute magnitude in Fig. 5 represents the total luminosity of the BCDs. It can be seen that the underlying hosts of our BCDs are consistent with the BCDs in Cairós et al. (2001) and Marlowe et al. (1997) in the luminosity-radius diagram. While the effective radius of the underlying host of our BCDs is immensely small compared to dIrrs and dEs, the central brightness is fainter than other BCDs but consistent with that of dIrrs and dEs.

A comparison of the structural parameters of BCDs with other dwarf galaxies at H bands is shown in Fig. 6. The upper row is for the inner Sérsic component and the bottom row for the outer exponential component. The empty red circles are our BCDs with one-component decomposition in this work and marked with ‘BCD1’. The solid red circles are BCDs with two-component decomposition and marked with ‘BCD2’. Janz et al. (2014) fit two-dimensional models to the images of dEs in Virgo cluster with both a one-component Sérsic model and a two-component model combining an inner Sérsic and an outer exponential component. About one third of the dEs in Janz et al. (2014) favour the simple one-component decomposition. The parameters of the one-component model for these dEs are also included in the comparison of underlying hosts in the bottom row of Fig. 6. The empty green squares represent dEs in the Virgo Cluster from Janz et al. (2014) with one-component decomposition and solid green squares for dEs with two-component decomposition. Although Noeske et al. (2003, 2005) only fit the outer regions of BCDs with an exponential function, their results should be comparable to the outer exponential component of the two-component decomposition. Therefore, we include these BCDs in the comparison of the exponential component in the bottom row of Fig. 6. Since dIrrs always have approximately exponential SBPs, we also include parameters for dIrrs for the comparison of underlying hosts in the bottom row in Fig. 6. Purple triangles represent dIrrs from Young et al. (2014) and McCall et al. (2012), who fit the whole galaxy with an exponential function. Since the parameters in McCall et al. (2012) were derived in the K_s band, we use a colour of $H - K = 0.1$ to obtain the equivalent surface brightness and magnitude at H band. We convert the supplied Vega magnitudes in literature to the AB photometric system with a conversion factor of 1.37 mag in the H band.

It should be noted that the absolute magnitudes of the inner and outer components are calculated by integrating the respective best-fitting profile of each component. This is different from the comparison in Fig. 5 where we used the absolute magnitude of the whole galaxy. It is interesting to note that the outer components of BCDs are in remarkable agreement with those of dEs. Their underlying hosts show a similar Sérsic index, extrapolated central surface brightness and effective radius. Moreover, all the outer regions of dwarf galaxies seem to follow a consistent luminosity-size relation, though the dIrrs tend to be slightly larger than BCDs at

the low-luminosity end. Janowiecki & Salzer (2014) found that the underlying hosts of BCDs are significantly smaller and centrally brighter than dIrrs. With more dIrrs in our comparison, the difference in structural parameters between BCDs and dIrrs seems to be less significant in the H band than in the B band. Unlike the outer components, the inner components of BCDs seem to have lower Sérsic index n and are fainter in the centre compared to dEs. Nevertheless, the size of the inner components of BCDs is consistent with those of dEs at a fixed luminosity.

5 DISCUSSION

Although an evolutionary connection between late-type and early-type dwarf galaxies was suggested over 30 yr ago (e.g. Lin & Faber 1983; Kormendy 1985; Davies & Phillipps 1988), the details remain vague. Some late-type dwarf galaxies located in dense regions may be environmentally transformed into dEs (Kormendy 1985; Boselli & Gavazzi 2006). Kormendy et al. (2009) and Kormendy & Bender (2012) showed that spheroidal galaxies are not dwarf elliptical but bulgeless S0 galaxies, with structural parameters consistent with the irregular galaxies. However, the difference in chemical abundances (Thuan 1985; Grebel et al. 2003) suggests that simple gas stripping is not enough to transform a dIrr into a dE. In this work, we investigate the possible evolutionary connection between late- and early-type dwarf galaxies by comparing their structural properties.

In the left-hand panel of Fig. 5, it can be seen that the central surface brightness of the underlying hosts of our BCDs are fainter than for other BCD samples but consistent with the dEs and dIrrs. This difference between different BCD samples may be due to the different fitting methods, since we fit the two-component model to the whole galaxy rather than only an exponential function to the outer region. In the right-hand panel of Fig. 5, the underlying hosts of BCDs seem to have distinctive structural properties compared to dEs and dIrrs. Since SBPs in the $F435W$ band only reach ~ 26 mag arcsec $^{-2}$, the structural properties may be affected by nebular emission from the star formation region as discussed in Micheva et al. (2013). Meanwhile, this distinctive distribution may also be due to the luminosities used for the underlying host of BCDs and other dwarf galaxies. Most comparisons in the literature, including Fig. 5 in this work, use the luminosity of a galaxy rather than the underlying host component. This is not representative for BCDs, since their luminosity in the B band includes a significant contribution of the central starburst region. If we replace the x -axis for our BCDs in Fig. 5 with the absolute magnitude of the outer component, more than half of the BCDs move to the region occupied by dIrrs. Therefore, we consider the difference of effective radius in the optical B band to be unphysical.

It is interesting to note that the structural parameters of the outer components of BCDs are in remarkable agreement with those of dEs when utilizing the deepest NIR imaging so far of BCDs. This consistency suggests that the underlying hosts of BCDs can not be distinguished from those of dEs and no significant change of structure is needed given the evolutionary connection between BCDs and dEs. In addition, we also find an approximately common luminosity-size

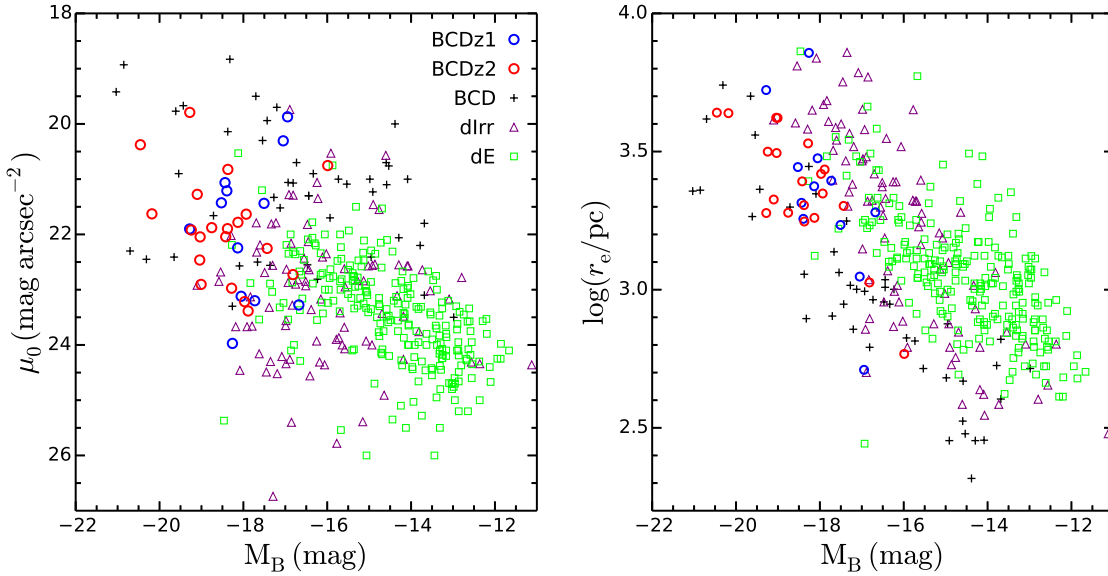


Figure 5. Comparison of structural parameters in the B band between the underlying hosts of BCDs and other dwarf galaxies. The blue circles represent our BCDs at redshift of 0.09 – 0.15 and are marked as ‘BCDz1’. The red circles are our BCDs at redshift of 0.15 – 0.25 and marked as ‘BCDz2’. The black crosses are the BCDs from Cairós et al. (2001) and Marlowe et al. (1997). Data for dIrrs are compiled from Patterson & Thuan (1996), van Zee (2000) and dEs from Binggeli & Cameron (1993).

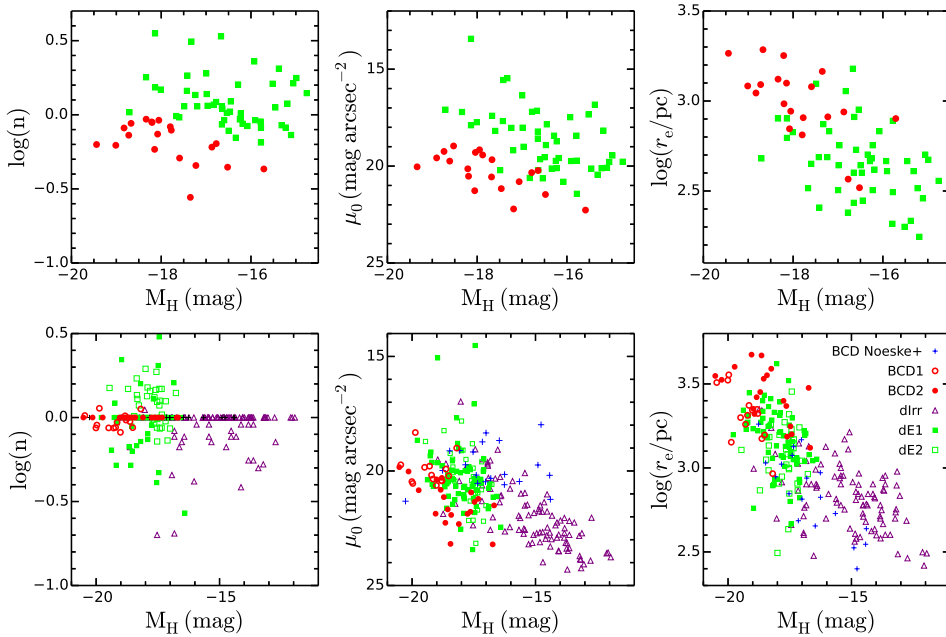


Figure 6. Comparison of structural parameters in the H band of BCDs and other type dwarf galaxies. The empty red circles are BCDs with one-component decomposition in this work and marked with ‘BCD1’. The solid red circles are BCDs with two-component decomposition and marked with ‘BCD2’. The blue crosses are BCDs from Noeske et al. (2003, 2005) and purple triangles are dIrrs from Young et al. (2014) and McCall et al. (2012). The empty green squares represent dEs in the Virgo Cluster from Janz et al. (2014) with one-component decomposition and marked with ‘dE1’. The filled green squares are dEs with two-component decomposition and marked with ‘dE2’. The parameters of inner Sérsic component are shown in the upper row and outer exponential component in bottom row.

Table 2. Parameters from SBP fitting in the *F435W*.

ID	One component					Inner component					Outer component			Preference ^c	
	<i>m</i> (mag)	<i>n</i>	μ_{435} (mag arcsec ⁻²)	r_e^a (kpc)	Q^b	<i>m</i> (mag)	<i>n</i>	μ_{435} (mag arcsec ⁻²)	r_e (kpc)	<i>m</i> (mag)	<i>n</i>	μ_{435} (mag arcsec ⁻²)	r_e (kpc)		Q
GN1	-19.0	0.78	22.7	3.1	0.08	-4.1	0.20	30.0	0.1	-19.0	1.00	22.4	3.3	0.11	one
GN2	-18.5	1.05	21.7	2.8	0.07	-14.4	0.20	24.0	0.6	-18.5	1.00	21.8	2.8	0.05	one
GN3	-18.7	1.09	20.4	1.3	0.23	-18.2	0.57	21.0	0.9	-17.8	1.00	22.0	1.9	0.07	two
GN4	-16.9	1.34	19.9	0.7	0.26	-15.2	0.56	20.6	0.4	-16.7	1.00	22.0	1.0	0.05	two
GN5	-19.3	1.26	22.4	5.3	0.06	-14.4	0.55	23.8	0.6	-19.2	1.00	22.8	5.0	0.04	one
GN6	-18.4	0.62	21.7	1.8	0.16	-17.1	0.20	23.5	1.8	-17.9	1.00	21.6	1.8	0.07	two
GN7	-16.6	1.71	20.5	1.1	0.29	-15.8	0.84	21.0	0.5	-16.0	1.00	23.6	1.9	0.08	two
GN8	-17.0	1.50	20.8	1.1	0.27	-16.7	0.87	21.3	0.7	-16.3	1.00	25.0	3.5	0.08	one
GN9	-18.3	2.15	21.7	6.5	0.22	-15.8	0.79	22.4	0.9	-18.1	1.00	24.2	7.2	0.05	two
GN10	-20.2	0.78	22.4	4.4	0.05	-4.2	0.20	30.0	0.1	-20.2	1.00	22.0	4.4	0.18	one
GN11	-19.3	1.24	20.3	1.9	0.14	-16.2	0.35	21.2	0.4	-19.2	1.00	20.9	2.1	0.11	one
GN12	-17.6	1.11	20.9	1.3	0.29	-17.2	0.52	21.5	1.0	-16.6	1.00	23.3	2.5	0.04	two
GN13	-18.4	0.89	22.7	2.5	0.16	-18.2	0.61	22.9	2.0	-18.9	1.00	26.6	20.5	0.05	one
GN14	-17.8	0.86	22.5	1.7	0.13	-17.1	0.49	23.1	1.3	-17.1	1.00	23.9	2.7	0.04	two
GN15	-16.7	1.21	20.2	0.5	0.25	-16.3	0.69	20.5	0.4	-15.7	1.00	23.0	1.1	0.08	two
GN16	-18.4	0.67	22.5	2.0	0.03	-17.6	0.44	23.4	1.9	-17.7	1.00	23.0	2.4	0.03	one
GN17	-19.2	0.81	22.7	3.2	0.09	-17.7	0.20	25.6	3.5	-18.9	1.00	22.6	2.9	0.09	one
GN18	-19.1	0.72	21.8	2.1	0.16	-19.0	0.48	22.1	1.9	-19.2	1.00	26.2	20.4	0.12	one
GN19	-19.2	2.29	20.1	3.6	0.28	-18.5	1.40	20.5	1.4	-18.9	1.00	25.0	9.8	0.13	two
GN20	-19.2	1.77	21.8	4.3	0.16	-16.5	0.82	22.3	0.7	-18.9	1.00	23.4	4.2	0.08	two
GS1	-16.2	1.47	20.3	0.7	0.37	-15.5	0.53	21.2	0.4	-15.2	1.00	23.2	1.2	0.08	two
GS2	-	-	-	-	-	-	-	-	-	-	-	-	-	-	-
GS3	-18.4	0.96	21.3	2.1	0.07	-18.3	0.81	21.5	1.9	-17.2	1.00	26.1	11.0	0.06	one
GS4	-17.9	0.88	21.8	1.6	0.15	-17.4	0.59	22.2	1.3	-16.9	1.00	23.7	2.6	0.07	two
GS5	-18.1	1.83	19.6	1.6	0.16	-17.1	1.02	20.0	0.6	-17.6	1.00	22.5	2.4	0.07	two
GS6	-18.3	1.61	21.5	2.6	0.27	-16.8	0.50	22.2	0.8	-18.0	1.00	23.5	3.4	0.06	two
GS7	-18.4	1.22	21.2	1.8	0.16	-17.3	0.42	24.6	2.8	-17.8	1.00	21.3	1.2	0.14	one
GS8	-17.5	1.34	22.1	1.9	0.09	-14.5	0.70	22.9	0.4	-17.4	1.00	22.9	2.0	0.05	two
GS9	-16.0	1.09	21.2	0.6	0.16	-13.2	0.20	27.3	1.3	-15.9	1.00	21.2	0.5	0.13	one
GS10	-17.9	1.22	22.3	2.2	0.14	-14.8	0.23	23.6	0.5	-17.8	1.00	22.8	2.3	0.08	one
GS11	-20.5	1.39	20.8	4.4	0.17	-20.2	1.02	21.1	3.3	-20.0	1.00	25.4	21.2	0.10	one
GS12	-17.5	1.01	21.6	1.7	0.10	-17.3	0.81	21.8	1.5	-17.0	1.00	25.7	9.0	0.09	one
GS13	-18.1	0.82	22.4	1.8	0.05	-18.1	0.82	22.4	1.8	-10.0	1.00	30.0	1.6	0.05	one
GS14	-18.0	1.69	19.7	1.4	0.20	-17.5	1.06	20.2	0.8	-17.1	1.00	23.4	3.0	0.05	two

Notes: ^aAll the surface brightness and radii correspond to the semi-major axes.^bfit quality: weighted quadratic sum of difference between observed and best-fitting model SBP.^cPreference for one-component model or two-component model.

relationship of different types of dwarf galaxies which suggests a unified structural evolution for dwarf galaxies.

In contrast to the outer disc, the inner components of BCDs are significantly different from those of dEs. However, it should be noted that the luminosity of the inner components of BCDs and dEs is fainter than the outer component by ~ 1.5 mag. With fewer data points, the structural parameters of the inner component may be more sensitive to the fitting procedure (such as initial value and parameter range) and less robust than those of the outer component. Nevertheless, if BCDs evolve to dEs rather than a simple cessation of star formation, passive fading could play a role. These likely inflict perturbations upon the stellar body, which tend to increase the concentration, and which could therefore lead to the higher central surface brightness, compacter size and higher Sérsic index of the inner component.

Actually, the structure of a galaxy varies at different wavelengths (Vulcani et al. 2014). For example, the effective radius decreases towards longer wavelengths. Therefore, the structural parameters of our BCDs derived at the observed

F435W or *F160W* band could be different from those for the rest-frame *B* or *H* band. Vulcani et al. (2014) investigated the wavelength-dependence of galaxy structure using a sample of bright low redshift galaxies. Although the dependence of dwarf galaxies may be different, we could roughly estimate the redshift effect in our comparison. For example, in the case of BCDs at $z \sim 0.25$, the *F435W* and *F160W* bands have restframe effective wavelengths of 3480 and 12800 Å, respectively. Although the effective radius is dependent on wavelength, the variance of wavelength is quite small with such narrow redshift range. In Fig. 13 of Vulcani et al. (2014), we find that the variances of effective radius are both generally small (< 5 percent by eye) in the wavelength range of 3480 – 4350 and 12800 – 16000 Å for galaxies with blue colour and $n < 2.5$. The difference of Sérsic index n could be slightly larger (see fig. 6 in Vulcani et al. 2014). In a word, we consider our result about the consistency between the structures of different types of dwarf galaxies to be robust.

Table 3. Parameters from SBP fitting in the $F160W$.

ID	One component					Inner component					Outer component			Preference	
	m (mag)	n	μ_{160} (mag arcsec $^{-2}$)	r_e (kpc)	Q	m (mag)	n	μ_{160} (mag arcsec $^{-2}$)	r_e (kpc)	m (mag)	n	μ_{160} (mag arcsec $^{-2}$)	r_e (kpc)		Q
GN1	-19.8	0.87	21.3	3.3	0.06	-19.3	0.68	21.7	2.7	-19.0	1.00	22.8	5.1	0.02	one
GN2	-18.7	0.97	20.8	2.1	0.10	-18.0	0.73	21.4	1.6	-18.0	1.00	22.2	2.9	0.05	one
GN3	-19.5	1.20	19.7	1.8	0.23	-18.9	0.62	20.4	1.2	-18.7	1.00	21.6	2.6	0.02	two
GN4	-18.1	1.12	19.6	0.9	0.12	-18.0	0.96	19.7	0.9	-16.1	1.00	25.4	5.1	0.09	one
GN5	-19.8	0.90	21.1	3.6	0.04	-19.5	0.82	21.4	3.2	-18.6	1.00	23.1	5.3	0.03	one
GN6	-19.2	0.87	20.2	1.8	0.06	-1.5	0.24	30.0	0.0	-19.2	1.00	19.9	1.8	0.16	one
GN7	-18.4	1.50	19.4	1.4	0.24	-17.9	0.92	19.9	0.9	-17.6	1.00	22.3	2.5	0.06	two
GN8	-18.3	1.34	19.1	1.0	0.26	-17.9	0.74	19.7	0.7	-17.3	1.00	21.9	1.8	0.03	two
GN9	-18.5	1.28	21.4	3.3	0.10	-15.6	0.43	22.6	0.8	-18.4	1.00	22.1	3.4	0.04	two
GN10	-20.4	1.03	20.4	3.4	0.08	-17.2	0.28	23.0	1.5	-20.4	1.00	20.6	3.5	0.05	two
GN11	-19.7	1.13	19.0	1.4	0.10	-19.7	0.97	19.2	1.4	-18.1	1.00	26.1	16.4	0.05	one
GN12	-17.9	1.09	20.2	1.2	0.23	-17.1	0.45	21.2	0.8	-17.4	1.00	21.4	1.5	0.03	two
GN13	-18.8	0.82	21.5	2.2	0.07	-18.4	0.63	21.8	1.8	-17.9	1.00	23.2	3.7	0.03	one
GN14	-18.2	0.92	21.4	1.6	0.15	-17.5	0.51	22.1	1.2	-17.5	1.00	22.7	2.3	0.03	two
GN15	-17.9	1.34	20.1	1.1	0.27	-17.7	0.79	20.5	0.8	-16.6	1.00	24.0	3.0	0.05	two
GN16	-19.1	0.87	20.9	2.1	0.05	-18.9	0.85	21.0	2.0	-16.6	1.00	24.1	3.1	0.04	one
GN17	-20.2	1.03	20.6	3.2	0.09	-16.7	0.24	23.3	1.2	-20.2	1.00	20.8	3.3	0.07	one
GN18	-19.5	0.90	20.6	2.2	0.13	-19.3	0.63	20.9	1.8	-18.3	1.00	24.0	6.5	0.03	two
GN19	-19.5	1.83	19.5	2.7	0.31	-18.7	0.81	20.1	1.1	-19.0	1.00	22.8	4.7	0.04	two
GN20	-20.0	1.49	19.9	3.1	0.19	-18.6	0.73	20.6	1.2	-19.6	1.00	21.7	4.0	0.05	two
GS1	-17.7	1.28	20.1	1.2	0.20	-16.8	0.60	20.9	0.9	-17.2	1.00	21.7	1.6	0.03	two
GS2	-18.7	1.02	21.4	2.2	0.05	-15.0	0.23	24.1	0.1	-18.7	1.00	21.5	2.3	0.03	one
GS3	-18.5	0.95	20.3	1.5	0.05	-16.0	0.20	23.4	0.2	-18.4	1.00	20.4	1.5	0.03	one
GS4	-19.3	0.87	20.4	2.0	0.10	-19.3	0.87	20.4	2.0	-10.1	1.00	30.0	2.6	0.10	one
GS5	-19.3	1.38	19.2	1.7	0.13	-18.0	0.89	19.8	1.0	-18.8	1.00	20.9	2.2	0.05	two
GS6	-18.9	1.63	20.8	3.3	0.21	-17.7	0.83	21.4	0.6	-18.5	1.00	23.1	4.7	0.05	two
GS7	-18.9	1.11	20.7	1.9	0.11	-16.5	0.44	22.4	0.3	-18.8	1.00	21.2	2.1	0.04	two
GS8	-19.0	1.37	20.3	2.3	0.16	-18.2	0.93	20.8	1.3	-18.3	1.00	22.6	3.6	0.04	two
GS9	-17.3	1.20	20.2	0.9	0.21	-16.6	0.64	20.8	0.4	-16.5	1.00	22.1	1.3	0.03	two
GS10	-18.8	1.27	20.8	2.5	0.15	-18.2	0.89	21.3	1.8	-18.1	1.00	23.1	3.9	0.05	two
GS11	-20.2	1.05	20.5	3.1	0.11	-18.1	0.58	22.1	1.3	-20.1	1.00	20.9	3.3	0.06	two
GS12	-19.1	0.94	20.7	2.4	0.06	-16.2	0.20	23.4	0.2	-19.0	1.00	20.8	2.5	0.05	one
GS13	-18.4	0.87	21.1	1.6	0.06	-18.4	0.87	21.1	1.6	-8.8	1.00	30.0	1.2	0.06	one
GS14	-19.2	1.61	18.7	1.7	0.21	-18.5	0.88	19.4	1.9	-18.6	1.00	21.6	2.8	0.03	two

6 SUMMARY

The main goal of this work is to study the structural properties of the underlying host of BCDs and compare them with other dwarf galaxies such as dIrrs and dEs. Unlike many previous works, which study dwarf galaxies in the nearby Universe, we selected 34 BCDs in the CANDEL GOODS-N and GOODS-S deep fields with a median redshift of 0.2. With deep NIR imaging from the CANDELS survey, we obtained the deepest NIR azimuthally averaged SBP of BCDs so far, reaching ~ 26 mag arcsec $^{-2}$ at the 3σ level. Then we fit the SBPs with one- and two-component Sérsic models. There are 16 of 33 BCDs in the $F435W$ band and 19 of 34 BCDs in the $F160W$ band which favour the two-component model.

Comparison between the structural properties of different types of dwarf galaxies offers an inspection of the possible evolutionary connections between them. We derived the structural properties of the underlying hosts of BCDs in the $F435W$ band and compared them to those of dEs and dIrrs. The effective radii of the underlying hosts of BCDs in the B band are smaller than those of dEs and dIrrs. This discrepancy is similar to findings in many previous works. However,

when we compare the structural properties in the H band, the difference between BCDs and other dwarf galaxies seems to be less significant. Furthermore, we find a remarkable agreement between the underlying hosts of BCDs and dEs in the H band. All dwarf galaxies, including dIrrs, seem to follow a similar luminosity-radius relationship, which suggests a unified structural evolution for dwarf galaxies. In contrast to the underlying hosts, the inner components of BCDs are significantly different from those of dEs. Passive fading from BCDs to dEs may be one of the possible mechanisms that can explain the different inner structure of BCDs and dEs.

There are two possible reasons for the disappearance of difference in structural parameters between BCDs and other dwarf galaxies in the H band. Micheva et al. (2013) suggested that the SBPs of BCDs for μ in the 24–26 mag arcsec $^{-2}$ range in the B band are affected by nebular emission and therefore may not trace the underlying stellar population distribution. Besides, comparison of the structures of dwarf galaxies using total luminosity is not representative for BCDs since the total luminosities of BCDs in the

B band include a significant contribution from the central star-forming region.

With deep NIR photometry and detailed SBP fitting, we conclude that the underlying hosts of BCDs can not be distinguished from those of dEs, and no significant change of structure is needed given the evolutionary connection between BCDs and dEs.

ACKNOWLEDGEMENTS

We are grateful for the referee's insightful suggestions and comments, which significantly improved the quality of this paper. This work is based on observations taken by the CANDELS Multi-Cycle Treasury Program and 3D-HST Treasury Program (GO 12177 and 12328) with the NASA/ESA *HST*, which is operated by the Association of Universities for Research in Astronomy, Inc., under NASA contract NAS5-26555. This work is supported by the National Natural Science Foundation of China (NSFC, nos. 11225315, 1320101002, 11433005 and 11421303), the Strategic Priority Research Program 'The Emergence of Cosmological Structures' of the Chinese Academy of Sciences (no. XDB09000000), the Specialized Research Fund for the Doctoral Program of Higher Education (SRFDP, no. 20123402110037), and the Chinese National 973 Fundamental Science Programs (973 programme) (2015CB857004).

REFERENCES

- Abraham, R. G., Nair, P., McCarthy, P. J., et al. 2007, *ApJ*, 669, 184
- Bertin, E., & Arnouts, S. 1996, *A&AS*, 117, 393
- Binggeli, B., & Cameron, L. M. 1993, *A&AS*, 98, 297
- Boselli, A., & Gavazzi, G. 2006, *PASP*, 118, 517
- Brammer, G. B., van Dokkum, P. G., Franx, M., et al. 2012, *ApJS*, 200, 13
- Cairós, L. M., Vílchez, J. M., González Pérez, J. N., Iglesias-Páramo, J., & Caon, N. 2001, *ApJS*, 133, 321
- Cairós, L. M., Caon, N., Papaderos, P., et al. 2003, *ApJ*, 593, 312
- Conselice, C. J. 2003, *ApJS*, 147, 1
- Davies, J. I., & Phillipps, S. 1988, *MNRAS*, 233, 553
- Gil de Paz, A., Madore, B. F., & Pevunova, O. 2003, *ApJS*, 147, 29
- Graham, A. W., & Driver, S. P. 2005, *PASA*, 22, 118
- Grebel, E. K., Gallagher, J. S., III, & Harbeck, D. 2003, *AJ*, 125, 1926
- Grogin, N. A., Kocevski, D. D., Faber, S. M., et al. 2011, *ApJS*, 197, 35
- Janowiecki, S., & Salzer, J. J. 2014, *ApJ*, 793, 109
- Janz, J., Laurikainen, E., Lisker, T., et al. 2014, *ApJ*, 786, 105
- Jedrzejewski, R. I. 1987, *MNRAS*, 226, 747
- Koekemoer, A. M., Faber, S. M., Ferguson, H. C., et al. 2011, *ApJS*, 197, 36
- Kong, X. 2004, *A&A*, 425, 417
- Kong, X., Charlot, S., Weiss, A., & Cheng, F. Z. 2003, *A&A*, 403, 877
- Kormendy, J. 1985, *ApJ*, 295, 73
- Kormendy, J., Fisher, D. B., Cornell, M. E., & Bender, R. 2009, *ApJS*, 182, 216
- Kormendy, J., & Bender, R. 2012, *ApJS*, 198, 2
- Kriek, M., van Dokkum, P. G., Labbé, I., et al. 2009, *ApJ*, 700, 221
- Kunth, D., & Östlin, G. 2000, *A&ARv*, 10, 1
- Li, Z.-Y., Ho, L. C., Barth, A. J., & Peng, C. Y. 2011, *ApJS*, 197, 22
- Lin, D. N. C., & Faber, S. M. 1983, *ApJL*, 266, L21
- Mannucci, F., Basile, F., Poggianti, B. M., et al. 2001, *MNRAS*, 326, 745
- Marlowe, A. T., Meurer, G. R., Heckman, T. M., & Schommer, R. 1997, *ApJS*, 112, 285
- Markwardt, C. B. 2009, *Analysis Software and Systems XVIII*, 411, 251
- Martins, L. P., Rodríguez-Ardila, A., Diniz, S., Gruenwald, R., & de Souza, R. 2013, *MNRAS*, 431, 1823
- McCall, M. L., Vaduvescu, O., Pozo Nunez, F., et al. 2012, *A&A*, 540, AA49
- Meyer, H. T., Lisker, T., Janz, J., & Papaderos, P. 2014, *A&A*, 562, AA49
- Micheva, G., Östlin, G., Bergvall, N., et al. 2013, *MNRAS*, 431, 102
- Noeske, K. G., Papaderos, P., Cairós, L. M., & Fricke, K. J. 2003, *A&A*, 410, 481
- Noeske, K. G., Papaderos, P., Cairós, L. M., & Fricke, K. J. 2005, *A&A*, 429, 115
- Papaderos, P., Loose, H.-H., Fricke, K. J., & Thuan, T. X. 1996, *A&A*, 314, 59
- Patterson, R. J., & Thuan, T. X. 1996, *ApJS*, 107, 103
- Prugniel, P., & Simien, F. 1997, *A&A*, 321, 111
- Sargent, W. L. W., & Searle, L. 1970, *ApJL*, 162, L155
- Skelton, R. E., Whitaker, K. E., Momcheva, I. G., et al. 2014, *ApJS*, 214, 24
- Thuan, T. X. 1985, *ApJ*, 299, 881
- van Zee, L. 2000, *AJ*, 119, 2757
- Vulcani, B., Bamford, S. P., Häußler, B., et al. 2014, *MNRAS*, 441, 1340
- Young, T., Jerjen, H., López-Sánchez, Á. R., & Koribalski, B. S. 2014, *MNRAS*, 444, 3052